Environmental
Science
Water Research & Technology

ROYAL SOCIETY
OF CHEMISTRY

PAPER

View Article Online
View Journal | View Issue

Check for updates

Cite this: *Environ. Sci.: Water Res. Technol.*, 2023, **9**, 2866

Received 13th June 2023,
Accepted 6th September 2023

DOI: 10.1039/d3ew00430a

rsc.li/es-water

Unlocking the effect of Zn^{2+} on crystal structure, optical properties, and photocatalytic degradation of perfluoroalkyl substances (PFAS) of Bi_2WO_6†

Mirabbos Hojamberdiev, *[a] Ana Laura Larralde, [bc] Ronald Vargas, [de] Lorean Madriz, [de] Kunio Yubuta,[f] Lokesh Koodlur Sannegowda, [g] Ilona Sadok, [h] Agnieszka Krzyszczak-Turczyn,[hi] Patryk Oleszczuk[i] and Bożena Czech*[i]

Bismuth tungstate (Bi_2WO_6) with a layered structure and visible light response exhibits excellent photocatalytic activity. To enhance its photocatalytic activity for the degradation of perfluoroalkyl substances (PFAS), Zn^{2+} is partially substituted for Bi^{3+} in the Bi_2WO_6 lattice in this study. Particularly, the effect of Zn^{2+} content (0–22.5 at%) on the crystal structure, optical property, and photocatalytic activity for the photodegradation of PFAS of Bi_2WO_6 is investigated. According to the Le Bail fits, the unit-cell volume is slightly reduced from 487.7 Å^3 to 480.8 Å^3 by the partial substitution of smaller Zn^{2+} (0.74 Å for CN = 6) for larger Bi^{3+} (1.03 Å for CN = 6) in the Bi_2WO_6 crystal lattice, and the solubility of Zn^{2+} in the Bi_2WO_6 lattice is found to be below 17.5 at%. The partial substitution of Zn^{2+} influences the self-aggregation of nanoparticles, Ostwald ripening, and self-organization of nanoplates, resulting in different morphologies. Although the optical bandgap energy of Bi_2WO_6 is not significantly altered upon the partial substitution of Zn^{2+}, the conduction and valence bands simultaneously shift upward. Among the $Bi_{2-x}Zn_xWO_{6+\delta}$ photocatalysts, 2.5 at% Zn^{2+}-substituted Bi_2WO_6 exhibits larger water oxidation photocurrent density (0.316 mA cm^{-2} at 1.23 V_{RHE}) and the highest photocatalytic activity for the photodegradation of PFH_xA (k_1 = 0.012 min^{-1}). The trapping experiments confirm that the photo-excited holes (h^+) and superoxide radicals ($O_2^{\bullet-}$) are the major reactive species involved in the photodegradation of PFH_xA. Liquid chromatography quadrupole time-of-flight mass spectrometry (LC-QTOF/MS) reveals that decarboxylation and defluorination are the main possible routes for the photodegradation of PFH_xA over $Bi_{2-x}Zn_xWO_{6+\delta}$ photocatalysts. Our findings suggest that the partial Zn^{2+}-to-Bi^{2+} substitution can enhance the photocatalytic activity of Bi_2WO_6 for the degradation of PFAS.

Water impact

The contamination of water with per- and poly-fluoroalkyl substances (PFAS) leads to adverse health effects because of their toxicity, extreme persistency, high mobility, and accumulative nature. The conventional water treatment process is ineffective in removing PFAS from contaminated water. The partial substitution of Zn^{2+} for Bi^{3+} in the Bi_2WO_6 crystal lattice can enhance the photocatalytic removal of PFAS from the model and real wastewater.

---

[a] *Institut für Chemie, Technische Universität Berlin, Straße des 17. Juni 135, 10623 Berlin, Germany. E-mail: hmirabbos@gmail.com*

[b] *Consejo Nacional de Investigaciones Científicas y Técnicas (CONICET), Buenos Aires, Argentina*

[c] *Instituto Nacional de Tecnología Industrial, Avenida General Paz 5445, San Martín (B1650WAB), Buenos Aires, Argentina*

[d] *Instituto Tecnológico de Chascomús (INTECH), Consejo Nacional de Investigaciones Científicas y Técnicas (CONICET), Avenida Intendente Marino, Km 8,2, Chascomús (B7130IWA), Provincia de Buenos Aires, Argentina*

[e] *Escuela de Bio y Nanotecnologías, Universidad Nacional de San Martín (UNSAM), Avenida Intendente Marino, Km 8,2, Chascomús (B7130IWA), Provincia de Buenos Aires, Argentina*

[f] *Department of Applied Quantum Physics and Nuclear Engineering, Kyushu University, Fukuoka 819-0395, Japan*

[g] *Department of Studies in Chemistry, Vijayanagara Sri Krishnadevaraya University, Cantonment, Vinayakanagara, Ballari, 583105, India*

[h] *Department of Chemistry, Institute of Biological Sciences, Faculty of Medicine, The John Paul II Catholic University of Lublin, Konstantynów 1J, 20-708 Lublin, Poland*

[i] *Department of Radiochemistry and Environmental Chemistry, Institute of Chemical Sciences, Faculty of Chemistry, Maria Curie-Skłodowska University in Lublin, 3 Maria Curie-Skłodowska Sq., 20-031 Lublin, Poland. E-mail: bozena.czech@mail.umcs.pl*

† Electronic supplementary information (ESI) available. See DOI: **https://doi.org/10.1039/d3ew00430a**

1. Introduction

Per- and poly-fluoroalkyl substances (PFAS) are a class of persistent, water-soluble synthetic organic compounds, including perfluorooctane sulfonate (PFOS) and perfluorooctanoic acid (PFOA).[1–3] Particularly, perfluorooctane sulfonate (PFOS) has been designated as one of the target chemicals by the Stockholm Convention on Persistent Organic Pollutants (POPs). PFAS have also adverse health effects due to their toxicity, persistency, mobility, and accumulative nature.[4] The United States Environmental Protection Agency (EPA) proposed maximum contaminant level goals (MCLG) of 4 ng L^{-1} and set a health recommendation of 70 ng L^{-1} for perfluorooctane sulfonate (PFOS) and perfluorooctanoic acid (PFOA).[5] PFAS are specifically characterized by having a fully or partially fluorinated carbon chain. Their high electronegativity and small ionic radius give them an extremely strong C–F bond (up to 544 kJ mol^{-1}) and high chemical and thermal stability, respectively.[6] Therefore, the degradation of PFAS remains challenging because of this strong C–F bond, risks associated with the persistency and toxicity of intermediates and final products, long treatment time, high energy requirement, and high capital cost.[7] For the elimination of PFAS, the conventional water treatment process has been found to be ineffective.[8]

Perfluorohexanoic acid (PFH_xA) is a short-chain, six-carbon perfluoroalkyl acid, and it is a principal contaminant, degradant, and metabolite linked to short-chain fluorotelomer-based compounds.[9,10] PFH_xA was detected in various water samples at concentrations reaching up to 1400 and 4000 ppb for drinking water and groundwater.[10] Therefore, the European Chemical Agency (ECHA) suggested listing PFH_xA as a "*substance of very high concern*" because of its extreme persistence, multiple sources, and high mobility in the aquatic environment.[11] Various techniques, including adsorption,[12] membrane filtration,[13] anion exchange resin,[14] foam fractionation,[15] advanced oxidation processes,[16] *etc.*, were applied for the removal of PFAS.

One of the methods applied for the removal of PFAS is physical adsorption.[17] In addition to its slow sorption rate because of the sluggish diffusion of PFAS molecules, physical adsorption simply converts PFAS from the liquid phase to the solid phase without completely mineralizing them. Therefore, to avoid secondary pollution, various redox treatment processes, including electrochemical,[18] photocatalytic,[19] photolytic,[20] photochemical,[21] sonochemical,[22] radiochemical,[23] thermochemical,[24] subcritical,[25] and plasma,[26] have been applied to completely mineralize PFAS compounds. Among the redox treatment processes, photocatalytic degradation is promising because of its operation under mind conditions and higher efficiency.[27] The homogeneous photocatalytic degradation of PFAS is based on the photo-Fenton process. Tang *et al.*[28] efficiently degraded PFAS by applying the photo-Fenton process and achieved more than 90% degradation and 53.2% defluorination after 5 h. Unlike P25-TiO_2 with low efficiency for PFAS degradation due to the recombination of photoexcited charge carriers,[29] In_2O_3 nanoporous nanospheres exhibited high and fast degradation efficiency towards PFAS (100% within 30 min) because of the presence of abundant oxygen vacancy defects ($V_{\ddot{O}}$).[30] Having an open layer structure, BiOCl with oxygen vacancies also exhibited a high defluorination efficiency (59.3%) after 3 h.[31] The sheaf-like β-Ga_2O_3 with nanoplates elongating in the [1 0 0] direction and a large number of nanopores exhibited a complete degradation of PFAS after 3 h of reaction.[32] The photodegradation of PFAS tightly bound on the surfaces of BiOCl and β-Ga_2O_3 followed the hole-oxidation path. The limiting factor of the oxidation process was found to be the electronic structures and reactive site distribution on specific surfaces, and facet engineering was suggested to improve the removal efficiency of PFAS.[33]

As one of the simplest members of the Aurivillius family ($Bi_2A_{n-1}B_nO_{3n+3}$), Bi_2WO_6 has an orthorhombic layer structure constructed from alternating $[Bi_2O_2]_n^{2n+}$ and perovskite-like $[WO_4]_n^{2n-}$ layers.[34] In general, this layer structure not only favors the separation and transfer of photoexcited charge carriers due to the built-in electric field vertical to the layer direction but also reduces the surface trapping of photoexcited charge carriers.[35] The valence band edge is more positively positioned,[36] providing the sufficient potential to thermodynamically drive a hole-mediated oxidation reaction. By changing the synthesis parameters and doping, the morphology and exposed facets of Bi_2WO_6 can be easily tuned, resulting in a large number of oxygen vacancies that act as electron scavengers and binding sites for adsorbates.[37]

Due to its capability to couple the highest occupied dopant states into the valence band, reduce the band gap, hamper the formation of midgap states in the forbidden band, and distort the crystal structure, Koteski *et al.*[38] and Ren *et al.*[39] computationally investigated the effect of Zn substituted partially for Bi and W lattice sites on the optical and electronic properties of Bi_2WO_6 using density functional theory (DFT), respectively. The partial substitution of Zn for W could narrow the optical bandgap energy without the direct presence of the localized defect states and affect the mobility of photoexcited charge carriers.[38] The partial substitution of Zn for Bi also led to band gap reduction due to the increase in the density of electrons and an upward shift of the conduction and valence band positions, revealing the possibility of the reaction of electrons with molecular oxygen to form active radicals.[39] Inspired by these two theoretical studies,[38,39] we aim to experimentally validate the effect of partial substitution of Zn for Bi on the crystal structure, optical properties, and photocatalytic activity for the degradation of perfluoroalkyl substances (PFAS) of Bi_2WO_6 in this study. The kinetics and mechanism of photodegradation of PFAS on Zn-substituted Bi_2WO_6 are also discussed.

2. Experimental

2.1. Synthesis

Pristine and Zn^{2+}-substituted Bi_2WO_6 photocatalysts were synthesized by a hydrothermal method.[40] For the synthesis of pristine Bi_2WO_6, $Bi(NO_3)_3{\cdot}5H_2O$ (98%, Merck) was dissolved in 5 mL of ethylene glycol (>99%, Merck), while $Na_2WO_4{\cdot}2H_2O$ (>99%, chemPUR) was dissolved in 5 mL of deionized water. For the synthesis of Zn^{2+}-substituted Bi_2WO_6, both $Bi(NO_3)_3{\cdot}5H_2O$ (98%, Merck) and $Zn(CH_3COO)_2{\cdot}2H_2O$ (>98%, Merck) were simultaneously dissolved in 5 mL of ethylene glycol (>99%, Merck), while $Na_2WO_4{\cdot}2H_2O$ (>99%, chemPUR) was dissolved in 5 mL of deionized water. Both solutions were then mixed under vigorous magnetic stirring, and the pH of the well-homogenized solution was adjusted to 7–9 by adding dropwise an aqueous solution of NaOH (98%, Alfa Aesar) and the mixture was transferred into a Teflon-lined stainless-steel autoclave (Parr Instrument GmbH). The hydrothermal reaction was carried out at 200 °C for 24 h. After the completion of the hydrothermal reaction, the resulting precipitate was washed and collected using a Universal 320 centrifuge (Andreas Hettich GmbH & Co. KG, 9000 rpm for 5 min), and dried at 80 °C for 12 h in a drying oven. The amount of Zn^{2+} substituted partially for Bi^{3+} in Bi_2WO_6 was controlled at 0, 1, 2.5, 7.5, 12.5, 17.5, and 22.5 at%. The synthesized powder samples were denoted as Zn0, Zn1, Zn2.5, Zn7.5, Zn12.5, Zn17.5, and Zn22.5 according to the content of substituted Zn^{2+}.

2.2. Characterization

The X-ray diffraction (XRD) patterns were acquired with a Panalytical X'Pert PRO diffractometer with Cu K_α radiation. The diffraction data were collected in a Bragg–Brentano geometry with a θ/θ-arrangement over an angular range of 2θ = 10–120° with a 0.026° step. Initial qualitative analysis of the XRD data was performed using the HighScore plus program (version 4.7) and compared to entries from the ICDD-PDF-2 powder pattern database. Le Bail fits were performed using the method implemented in the FULLPROF Suite[41] in order to determine the lattice parameters and proper fit of the crystalline phases. The microstructures of the synthesized samples were examined using a Carl Zeiss GeminiSEM 500 NanoVP scanning electronic microscope (SEM). The bright-field and lattice images and selected-area electron diffraction (SAED) patterns were obtained using an EM-002B high-resolution transmission electron microscope (TOPCON) at an accelerating voltage of 200 kV. The UV-vis diffuse reflectance spectra were recorded on an Evolution 220 UV/vis spectrometer (Thermo Fisher Scientific).

Photoelectrochemical tests were performed with a DropSens μSTAT200 potentiostat in 0.1 M Na_2SO_4 deoxygenated water solution (50 μL). Irradiation was provided with a solar light LED. The $Bi_{2-x}Zn_xWO_{6+\delta}$ photocatalysts were dip-coated on the carbon surface (0.13 cm^2) of the working electrode of the commercial screen-printed electrode (DS110), following the procedure previously reported elsewhere.[42,43] Linear scanning voltammetry (LSV) at 5 mV s^{-1} from 0.2 to 1.4 V (V *vs.* Ag–AgCl) and chronoamperometry (CA) at 1.4 V (*vs.* Ag–AgCl) for 1 h were conducted.

2.3. Photocatalytic activity tests

The photocatalytic activity of pristine and Zn^{2+}-substituted Bi_2WO_6 samples was evaluated for the degradation of polyfluoroalkyl and perfluoroalkyl substances (PFAS). First, 0.4 mg L^{-1} of the synthesized sample was dispersed in an aqueous solution of PFH_xA (5 mg L^{-1}) in the photochemical reactor (0.7 L, Heraeus) in the dark to achieve adsorption–desorption equilibrium for 30 min. Then, a 150 W mercury lamp, which was vertically placed in the center of the photoreactor, with emitting radiation centered at 500–550 nm, an intensity of 7.31–7.53 mW cm^{-2}, and a photon flux of 20.83×10^{19} m^2 s^{-1} was turned on. During the photocatalytic reaction, an aliquot was collected at different times (−30, 0, 5, 15, 30, 45, 60, and 120 min), filtered, and analyzed by High-Performance Liquid Chromatography (1200 Series Gradient HPLC System, Agilent Technologies). The extracted ion chromatograms of PFH_xA and $^{13}C_6$-PFH_xA are shown in Fig. S1.† The details of the instrumentation and analysis conditions of HPLC are given in the ESI.† The blank test conducted without any photocatalyst sample revealed that PFH_xA was not decomposed under visible light irradiation as a stable long-chain PFAS decomposition product.[44]

The ratio of the PFH_xA concentrations before and after the photocatalytic reactions C/C_0 was used to indicate the amount of PFH_xA photocatalytically removed from the aqueous solution. The effects of various parameters, such as the initial pH of PFH_xA-containing aqueous solution (controlled using 0.1 mol L^{-1} NaOH or 0.1 mol L^{-1} HCl), competing ions (Cl^-, NO_3^-, and $H_2PO_4^-$ from respective sodium salts with a concentration of 5×10^{-3} mol L^{-1}), and water matrix (distilled water – DW, tap water – TW, and treated wastewater – TWW) on the efficiency of the photocatalytic degradation of PFH_xA over pristine and Zn^{2+}-substituted Bi_2WO_6 photocatalysts were studied. TWW was collected from the municipal wastewater treatment plant "Hajdów" in Lublin, which is a mechanical-biological wastewater treatment facility with increased removal of biogenic compounds (nitrogen and phosphorus) from wastewater. TWW was characterized by significantly reduced biological (5.7 mg L^{-1}) and chemical (35.1 mg L^{-1}) oxygen demands, total suspended solids (up to 6.4 mg L^{-1}), and total nitrogen (10.72 mg L^{-1}) and phosphorous (0.27 mg L^{-1}) contents. TW was characterized by total organic carbon (<3 mg L^{-1}), chloride (35 mg L^{-1}), nitrate (<2 μg L^{-1}), and sulfate (41 mg L^{-1}) contents, and pH of 7.2.

Toxicity towards marine bacteria (*Aliivibrio fischeri*) was also evaluated based on the inhibition of bioluminescence using the Microtox® test.[45] The luminescence inhibition was determined after 5 min and 15 min of exposure of *Aliivibrio fischeri* to the water samples before and after the photocatalytic reaction according to the standard protocol

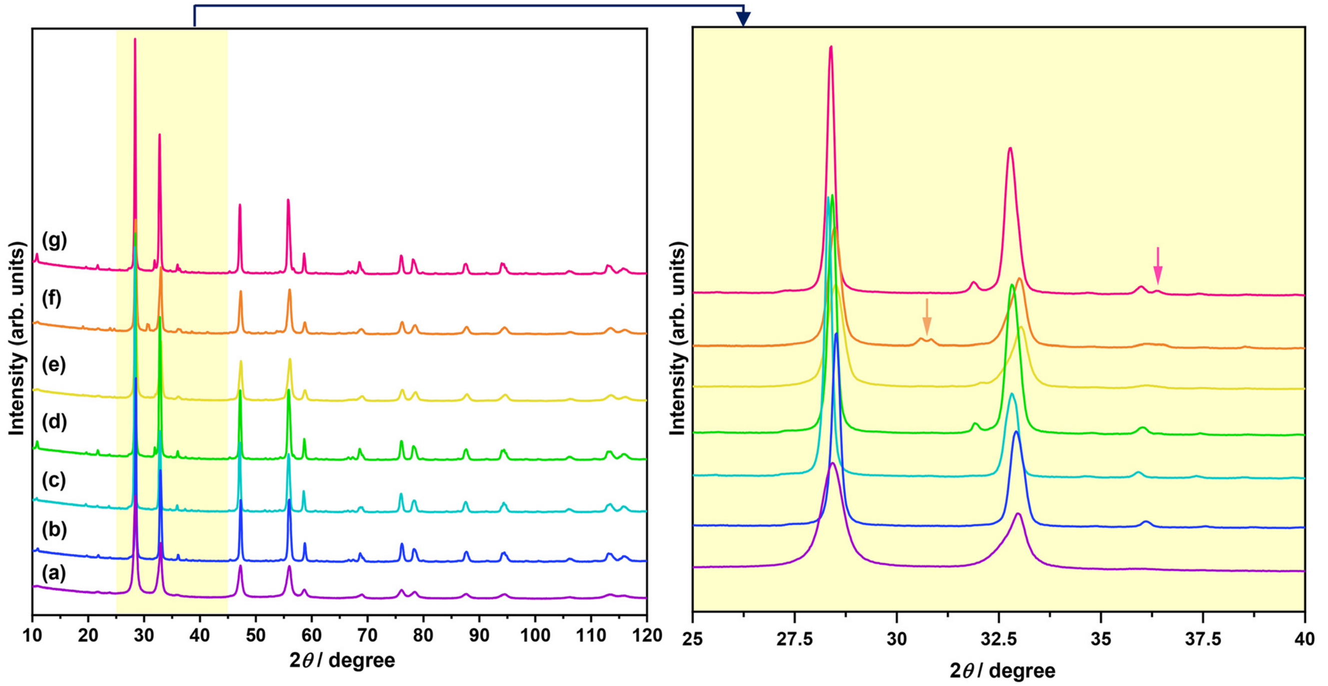

Fig. 1 XRD patterns of $Bi_{2-x}Zn_xWO_{6+\delta}$ powders with varying contents of Zn^{2+} substituent: (a) Zn0, (b) Zn1, (c) Zn2.5, (d) Zn7.5, (e) Zn12.5, (f) Zn17.5, and (g) Zn22.5. The orange and magenta arrows indicate the reflections belonging to $ZnWO_4$ and ZnO, respectively.

(Microtox®, 1995) in a Microtox M500 analyzer with the Omni software. All obtained data were expressed with the standard deviation.

3. Results and discussion

3.1. Material characterization

The XRD patterns of $Bi_{2-x}Zn_xWO_{6+\delta}$ photocatalysts with varying contents of Zn^{2+} substituent are shown in Fig. 1. The main reflections in the XRD patterns of $Bi_{2-x}Zn_xWO_{6+\delta}$ photocatalysts can be indexed to the orthorhombic Bi_2WO_6 phase with a space group of $Pca2_1$ and lattice parameters of a = 5.4370 Å, b = 16.4300 Å, and c = 5.4580 Å (ICSD# 98-006-7647). The $Bi_{2-x}Zn_xWO_{6+\delta}$ photocatalysts maintained the phase purity up to 12.5 at% Zn^{2+} (sample Zn12.5), and a further increase in the Zn^{2+} content affected the phase purity of the $Bi_{2-x}Zn_xWO_{6+\delta}$ photocatalysts. That is, additional reflections corresponding to the monoclinic $ZnWO_4$ phase with a space group of $P2/c$ and lattice parameters of a = 4.5160 Å, b = 5.5210 Å, and c = 4.7990 Å (ICSD# 98-016-2236) and the hexagonal ZnO phase with a space group of $P6_3mc$ and lattice parameters of a = 3.2420 Å, b = 3.2420 Å, and c = 5.1880 Å (ICSD# 98-006-5119) appeared at 17.5 and 22.5 at% Zn^{2+} (samples Zn17.5 and Zn22.5), respectively. It can be stated that the solubility of Zn in the Bi_2WO_6 matrix is below 17.5 at%. Table 1 summarizes the results from the Le Bail fits and the agreement factors of the calculations. Profile matching of the $Bi_{2-x}Zn_xWO_{6+\delta}$ photocatalysts with 17.5 and 22.5 at% Zn^{2+} (samples Zn17.5 and Zn22.5) was performed using two different phases (Fig. 2a and b). The goodness of the agreement factors confirms a satisfactory fit of the $ZnWO_4$ and ZnO phases. The calculated unit-cell volume decreased with increasing the Zn^{2+} content up to 12.5 at% (Fig. S2†). This is due to the fact that the ionic radius of Zn^{2+}

Table 1 Lattice parameters and agreement factors of the Le Bail fit of the $Bi_{2-x}Zn_xWO_{6+\delta}$ photocatalysts

Sample	Zn0	Zn1	Zn2.5	Zn7.5	Zn12.5	Zn17.5		Zn22.5	
Crystalline phase	Bi_2WO_6	Bi_2WO_6	Bi_2WO_6	Bi_2WO_6	Bi_2WO_6	Bi_2WO_6	$ZnWO_4$	Bi_2WO_6	ZnO
Space group	$Pca2_1$	$Pca2_1$	$Pca2_1$	$Pca2_1$	$Pca2_1$	$Pca2_1$	$P2/c$	$Pca2_1$	$P6_3mc$
a (Å)	5.4482 (7)	5.4318 (2)	5.4384 (2)	5.4355 (2)	5.4280 (4)	5.4239 (3)	4.684 (1)	5.4354 (2)	3.2255 (7)
b (Å)	16.423 (2)	16.4185 (5)	16.4278 (6)	16.4299 (5)	16.426 (1)	16.4090 (9)	5.724 (1)	16.4351 (6)	
c (Å)	5.4507 (6)	5.4473 (2)	5.4551 (2)	5.4511 (2)	5.3924 (3)	5.3829 (3)	4.9318 (8)	5.4549 (2)	5.288 (3)
β (°)	—	—	—	—	—	—	90.58 (2)	—	—
Volume (Å^3)	487.7 (1)	485.81 (3)	487.36 (3)	486.81 (3)	480.80 (5)	479.08 (4)	132.22 (5)	485.56 (3)	47.65 (3)
R_p	2.19	2.34	2.55	2.55	2.62	2.51	7.50	2.47	5.83
R_{wp}	3.15	3.23	3.90	3.66	3.53	3.45	7.30	3.60	6.41
R_{exp}	1.53	1.68	1.66	1.57	1.67	1.68	3.55	1.59	2.83
χ^2	4.26	3.71	5.54	5.39	4.47	4.23	4.23	5.14	5.14

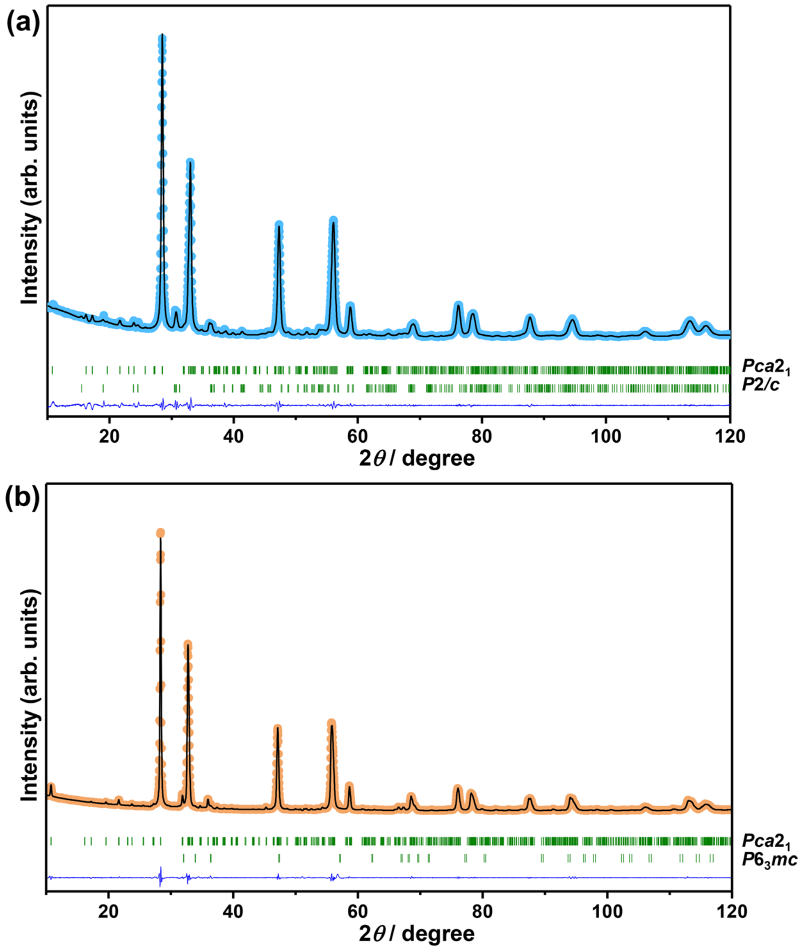

Fig. 2 Le Bail fit of XRD patterns of (a) Zn17.5 and (b) Zn22.5 samples. The blue line indicates the difference between observed (*dots*) and calculated (*black line*) intensities and the vertical green bars are the Bragg positions of *Pca*2_1 and *P*2/*c* for Zn17.5 and *Pca*2_1 and *P*6_3*mc* for Zn22.5.

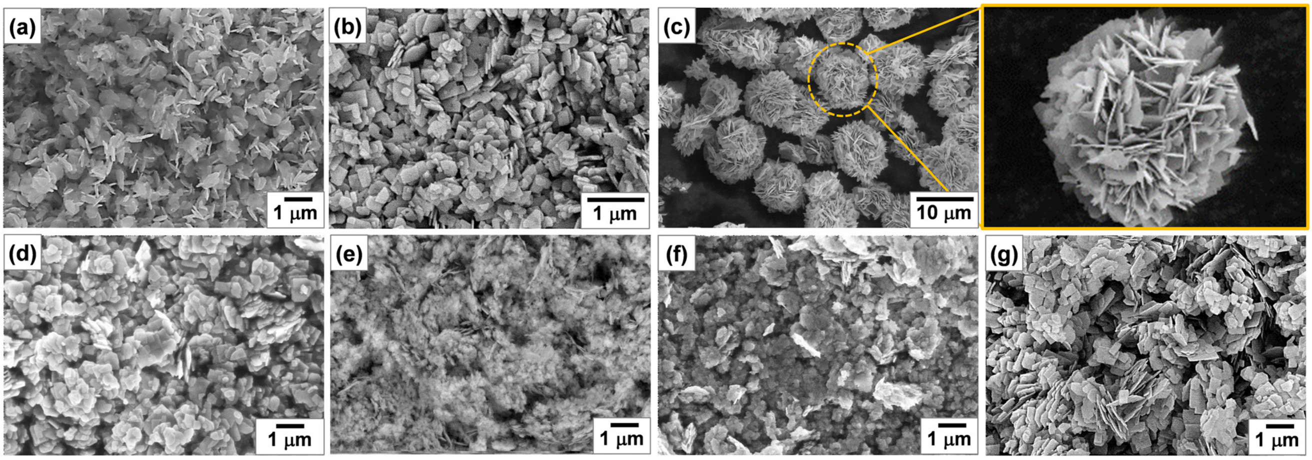

Fig. 3 SEM images of $Bi_{2-x}Zn_xWO_{6+\delta}$ powders with varying contents of Zn^{2+} substituent: (a) Zn0, (b) Zn1, (c) Zn2.5, (d) Zn7.5, (e) Zn12.5, (f) Zn17.5, and (g) Zn22.5.

(0.74 Å) is much smaller than that of Bi^{3+} (1.03 Å) in a six-fold coordination.[46] Thus, the partial substitution of Zn^{2+} for Bi^{3+} in the crystal lattice of Bi_2WO_6 contracts the unit-cell volume. Interestingly, the unit-cell volume was slightly increased in the $Bi_{2-x}Zn_xWO_{6+\delta}$ photocatalysts containing 22.5 at% Zn^{2+}. In the case of the $Bi_{2-x}Zn_xWO_{6+\delta}$ photocatalysts containing 17.5 and 22.5 at% Zn^{2+} (samples Zn17.5 and Zn22.5), the unit-cell volumes could not be properly estimated due to the simultaneous presence of Zn^{2+} in Bi_2WO_6 and minor impurity phases.

Fig. 3 shows the SEM images of $Bi_{2-x}Zn_xWO_{6+\delta}$ photocatalysts with varying contents of Zn^{2+} substituent. Unlike the Bi_2WO_6 particles with three-dimensional morphologies,[47–49] pristine Bi_2WO_6 (sample Zn0) synthesized by a hydrothermal method in this study possesses a platelet morphology with an average diameter of <600 nm (Fig. 3a), which was possibly formed by the self-assembly of ultrathin nanosheets. At 1 at% Zn^{2+} substituent, the platelet morphology was altered, and large anisotropic nanoplates with irregular shapes were formed due to the dominance of the dissolution–recrystallization (Oswald ripening) process over self-assembly (Fig. 3b). According to a recent study by Iversen and co-workers,[50] the preferential growth of Bi_2WO_6 nanoplates under hydrothermal conditions is governed by the initial presence of $Bi_2O_2^{2+}$ molecular complexes that interact with WO_4^{2-} tetrahedra, forming disordered $Bi_{0.933}W_{0.067}O_{1.6}$, and when there are sufficient WO_4^{2-}units intertwined the Bi_2WO_6 nanoplates are eventually formed by the sideways addition of units in the *ac* plane, which has a three times faster growth rate than the *b* direction. Strikingly, flower-like microstructures were formed when the content of Zn^{2+} substituent was set to 2.5 at% (Fig. 3c). Clearly, 2.5 at% Zn^{2+} substituent balanced the self-aggregation of nanoparticles, Ostwald ripening, and self-organization of nanoplates with high anisotropic surface energy,[51] resulting in flower-like microstructures. By adjusting the amount of Zn^{2+} substituent to 7.5, 12.5, and 17.5 at%, the governing roles of Oswald ripening and self-organization were subdued, forming some nanoplates along with nanoparticles (Fig. 3d–f). A further increase in the concentration of Zn^{2+} to 22.5 at% gave rise to the Ostwald ripening process but not to the self-organization process (Fig. 3g). It is evident that the partial substitution of Zn^{2+} for Bi^{3+} in the Bi_2WO_6 crystal lattice changed the content of $Bi_2O_2^{2+}$ molecular complexes interacting with WO_4^{2-} tetrahedra, surface atomic structure, and surface free energy, which ultimately affected the particle morphology of $Bi_{2-x}Zn_xWO_{6+\delta}$ photocatalysts.

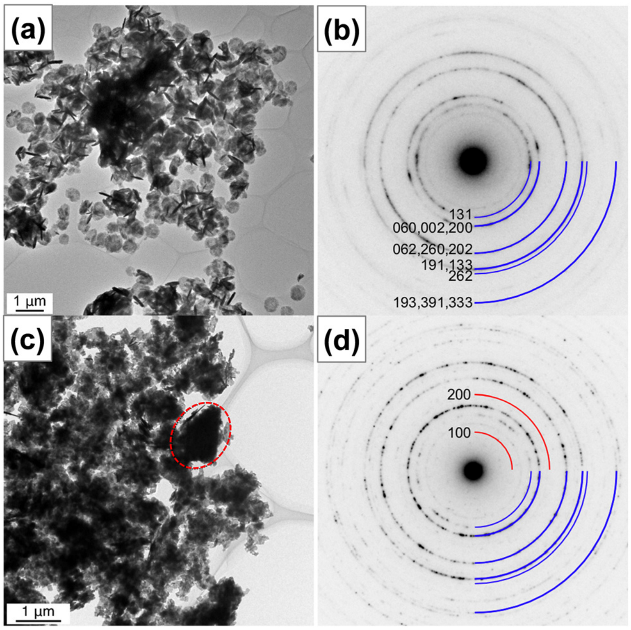

Fig. 4 TEM images (*left*) and SAED patterns (*right*) of Zn0 (a and b) and Zn17.5 (c and d).

Further, the nanostructures were characterized by transmission electron microscopy. Fig. 4 shows the bright-field TEM and HRTEM images and SAED patterns of pristine (sample Zn0) and 17.5 at% Zn^{2+}-substituted (sample Zn17.5) Bi_2WO_6 photocatalysts. In Fig. 4a, the low-magnification TEM image of sample Zn0 shows that pristine Bi_2WO_6 is in the form of platelets with a diameter of 580 nm and a thickness of about 75 nm. The high-magnification TEM image of sample Zn0 in Fig. S3a† confirms that the platelets were formed by the self-assembly of ultrathin nanosheets. The observed lattice fringes with a *d*-spacing value of 0.390 nm in Fig. S3b† manifest that the ultrathin nanosheets have exposed (1 3 0) facets along the $[\bar{3}\ 1\ 6]$ direction. No obvious defects are noticed in the examined area, suggesting the high crystallinity of ultrathin nanosheets. In the corresponding selected area electron diffraction pattern (Fig. 4b), a ring diffraction pattern can be seen due to the random orientation of crystallites. The observed Debye–Scherrer ring patterns are indexed to the different Miller indices of orthorhombic Bi_2WO_6. In Fig. 4c, the bright-field TEM image of sample Zn17.5 indicates the change in the nanostructure upon 17.5 at% Zn^{2+} substitution and the formation of large irregular particles, which are enclosed by a dotted oval, along with ultrathin nanosheets. In the corresponding selected area electron diffraction pattern in Fig. 4d, the Debye–Scherrer ring patterns are indexed to the different Miller indices of orthorhombic Bi_2WO_6 and monoclinic $ZnWO_4$, which is consistent with the XRD result.

The optical properties of the synthesized samples were analyzed by UV-vis spectroscopy. Fig. 5a shows the UV-vis diffuse reflectance spectra of $Bi_{2-x}Zn_xWO_{6+\delta}$ photocatalysts with varying contents of Zn^{2+} substituent. A typical absorption edge at approximately 445 nm was noted for pristine Bi_2WO_6 (sample Zn0), which corresponds to an optical bandgap energy of 2.78 eV according to the Kubelka–Munk function *vs.* the energy of absorbed light. This is due to the transition from filled anti-bonding states, formed by the hybridization of Bi 6s and O 2p orbitals at the top of the valence band to the empty W 5d orbitals in the conduction band.[52] With increasing the Zn^{2+} content to 1, 2.5, 7.5, and 12.5 at%, the absorption edges of $Bi_{2-x}Zn_xWO_{6+\delta}$ photocatalysts were slightly redshifted toward 453, 475, 451, and 448 nm, respectively. A slight reduction in the optical bandgap energy upon partial substitution of Zn^{2+} for Bi^{3+} stemmed from the merging and coupling of the highest occupied substituent states (the Zn 3d-levels) into the valence band[39] and the split-off of states near the top of the valence band as a result of a substituent–host interaction (Zn–3d-states and O–2p-state).[38] The partial substitution led to the upward shift of the conduction band minimum and valence band maximum.[39] A further increase in the Zn^{2+}

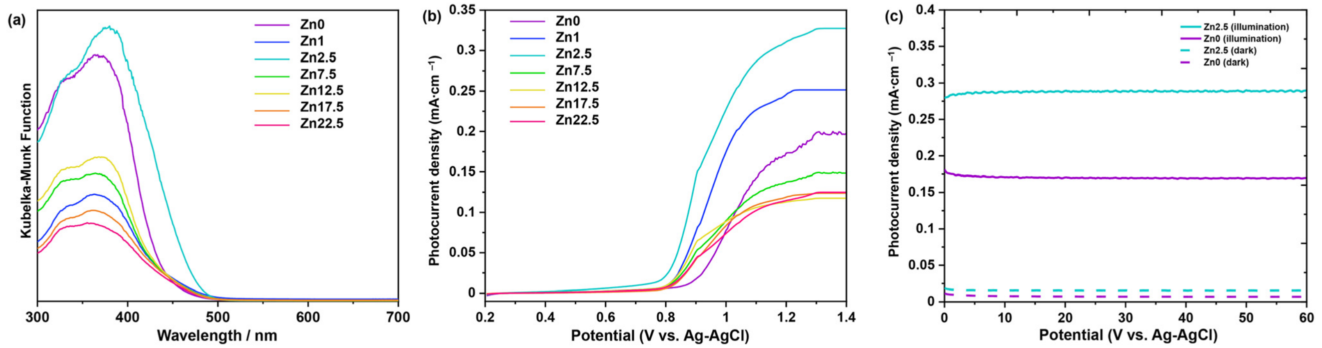

Fig. 5 (a) UV-vis diffuse reflectance spectra of $Bi_{2-x}Zn_xWO_{6+\delta}$ powders with varying contents of Zn^{2+} substituent. Photoelectrochemical results of $Bi_{2-x}Zn_xWO_{6+\delta}$ as photoanodes in 0.1 M Na_2SO_4 deoxygenated water solution: LSV (b) and CA (c) at 1.4 V (V *vs.* Ag–AgCl) for Zn0 and Zn2.5.

content to 17.5 and 22.5 at% resulted in the blueshift in the light absorption due possibly to the existence of $ZnWO_4$ and ZnO with absorption edges at about 355 nm (ref. 53) and 385 nm,[54] respectively. Among the $Bi_{2-x}Zn_xWO_{6+\delta}$ samples, 2.5 at% Zn^{2+}-substituted Bi_2WO_6 is more effective in absorbing visible light, which is important for enhancing the visible-light-driven photocatalytic activity. Unlike in previous studies,[38,55,56] no background absorption beyond the absorption edges was observed upon partial substitution of Zn^{2+}, suggesting the absence of deep impurity states within the band gap.

The photoelectrochemical studies allow the elucidation of the characteristics of a photocatalyst for the conversion of light energy in chemical reactions. Fig. 5b presents the LSV results. The LSV response of $Bi_{2-x}Zn_xWO_{6+\delta}$ photocatalysts is due to the photoinduced oxidation of water and is qualitatively consistent with previous reports.[57,58] Under light illumination, all the photocatalysts define a photocurrent with the following order: Zn2.5 > Zn1.0 > Zn0 > Zn7.5 > Zn12.5 = Zn17.5 = Zn22.5. Therefore, Bi_2WO_6 partially substituted with 2.5 at% Zn^{2+} exhibits the highest water oxidation photocurrent density (0.316 mA cm^{-2} at 1.23 V_{RHE}), projecting itself as a photocatalyst capable of effectively promoting different photo-redox reactions. In general, the potential at which the photocurrent begins to be representative is relatively positive for all the samples, suggesting that charge carrier recombination dominates at low overpotentials. However, as the potential increases, the photocurrent is observed to increase to a *pseudo*-steady value at very high overpotentials. The latter is evidence that electron transfer phenomena become important at higher overpotentials, since polarization allows photo-excited electrons to be collected, effectively slowing down the recombination process. It is worth mentioning that Zn0 and Zn2.5 define the CA response with a constant photocurrent for 1 h (Fig. 5c), indicating the stability of the photocatalysts under light irradiation and high polarization conditions. Therefore, the $Bi_{2-x}Zn_xWO_{6+\delta}$ photocatalysts studied have a consistent photoelectrochemical response that results from the interplay of light absorption and the balance between recombination and charge transfer processes.[59]

3.2. Photocatalytic degradation of PFH_xA

The photocatalytic activity of $Bi_{2-x}Zn_xWO_{6+\delta}$ photocatalysts was evaluated for the photodegradation of PFH_xA in an aqueous solution for 120 min. Fig. 6 shows the reaction time course of the photodegradation of PFH_xA over $Bi_{2-x}Zn_xWO_{6+\delta}$ photocatalysts. As shown in Fig. 6a, the content of the Zn^{2+} substituent influenced the photodegradation kinetics of PFH_xA over $Bi_{2-x}Zn_xWO_{6+\delta}$ photocatalysts. Although the photodegradation of PFH_xA was slow, the pronounced change in the concentration of PFH_xA was noted in the first 45 min under light irradiation. The highest photodegradation rate of PFH_xA was observed for sample Zn2.5 (up to 57%), followed by Zn1.0 (40%), Zn0 (37%), and Zn7.5 (32%). Samples Zn12.5, Zn17.5, and Zn22.5 are characterized to have a lower photodegradation rate of PFH_xA (<30%). Clearly, 2.5 at% Zn^{2+} substitution was favorable to enhance the adsorption and photodegradation of PFH_xA over $Bi_{2-x}Zn_xWO_{6+\delta}$ photocatalysts due to the optimum concentration of oxygen vacancies.

Recently, Lovisa *et al.*[55] experimentally studied the impact of partial substitution of Zn for Bi on the photocatalytic and photoluminescence properties of Bi_2WO_6 and found that Zn could not effectively favor the photocatalytic property but the photoluminescence property due to the increase in the recombination rate of photoexcited charge carriers in the oxygen vacancy-related defects. On the contrary, In_2O_3 nanostructures with pores showed high photocatalytic activity toward PFAS degradation because of the presence of abundant oxygen vacancy defects on their surface,[30] which received an O atom from the –COOH group of PFOA molecules, forming a close contact with In_2O_3 and improving the charge transfer and photocatalytic activity under UV irradiation. The oxygen vacancy in the BiOI microspheres was tuned by Zn^{2+} substitution and an increase in the concentration of oxygen vacancies enhanced the photocatalytic activity for NO removal.[60] Also, the flower-like microstructures of sample Zn2.5 permit multiple light scattering and offer a longer optical path, which improves the efficiency of light harvesting and increases the number of photo-excited charge carriers available for the

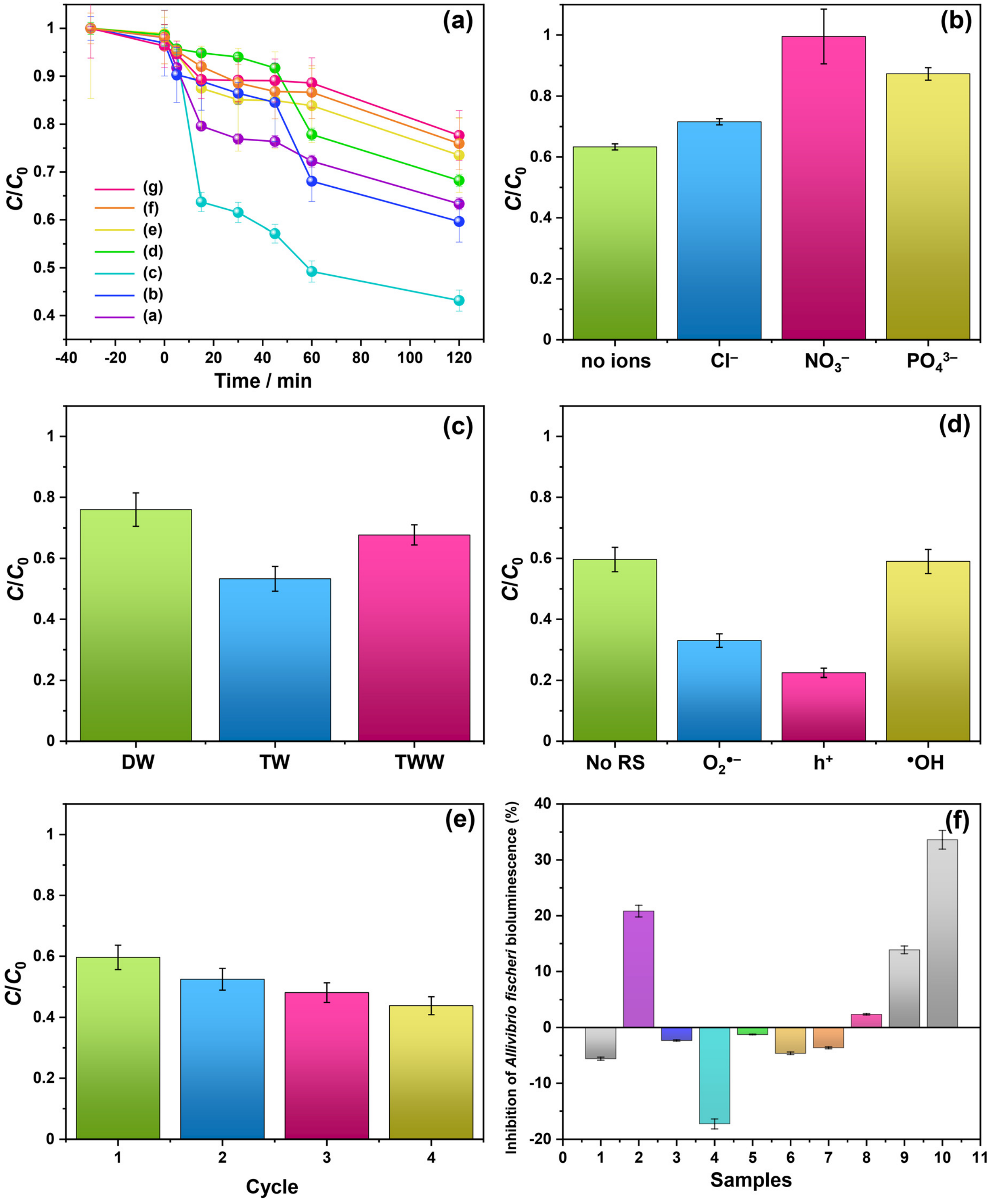

Fig. 6 Kinetics of photocatalytic degradation of PFH$_x$A over $Bi_{2-x}Zn_xWO_{6+\delta}$ powders (a). Effects of inorganic ions in the presence of 3 mmol L^{-1} sodium salts (b), water matrix (c), and radical scavengers (d) on photocatalytic degradation of PFH$_x$A over sample Zn2.5. (e) Toxicity test of PFH$_x$A-containing water samples before (1) and after photocatalytic treatment with (2) Zn0, (3) Zn1, (4) Zn2.5, (5) Zn7.5, (6) Zn12.5, (7) Zn17.5, and (8) Zn22.5 and after photocatalytic treatment in TW (9) and TWW (10) water samples (f).

photodegradation of PFH$_x$A. Similarly, flower-like microspheres of Bi_2WO_6 exhibited superior photocatalytic activity for the photodegradation of RhB in comparison to the plate-like and clew-like structures due to their efficient separation and transfer of photo-excited charge carriers and enhanced light-harvesting efficiency.[61] Previously, P25-TiO_2 exhibited 31.1% degradation efficiency and 3.3% defluorination efficiency for PFOA,[62] while In_2O_3 with graphene showed 100% degradation efficiency and 60.9% defluorination efficiency for PFOA although it requires a thermal treatment at 400 °C.[63] As shown in Table S1 in the ESI,† although some photocatalysts and processes showed

Table 2 Kinetic parameters of photocatalytic degradation of PFH_xA over $Bi_{2-x}Zn_xWO_{6+\delta}$ photocatalysts

Photocatalyst	k_1 (×10^3) min^{-1}	$t_{1/2}$ (min)	R^2	k_2 (×10^3) (mg g^{-1} min^{-1})	R^2
Zn0	5.32	130	0.9690	9.10	0.9686
Zn1.0	5.23	133	0.9456	12.13	0.9289
Zn2.5	12.24	57	0.9923	17.64	0.9980
Zn7.5	3.49	198	0.9032	8.67	0.8855
Zn12.5	3.19	217	0.9844	6.86	0.9870
Zn17.5	3.05	227	0.9734	6.86	0.9684
Zn22.5	2.39	290	0.9809	5.66	0.9756

high efficiency in the degradation of PFAS, they were conducted under UV light irradiation. In contrast, 2.5 at% Zn^{2+}-substituted Bi_2WO_6 exhibited a 57% removal efficiency of PFH_xA in 45 min under visible light irradiation. Apparently, the photocatalytic removal of PFH_xA by $Bi_{2-x}Zn_xWO_{6+\delta}$ photocatalysts followed a *pseudo*-first-order kinetics, implying that the adsorption process was a rate-limiting step of the reaction, and the highest *pseudo*-first-order kinetic constant (k_1) was observed for sample Zn2.5 (0.012 min^{-1} in Table 2). With increasing the concentration of Zn^{2+} substituent, the k_1 value gradually decreased. Table 2 shows the kinetic parameters, such as k_1, half-life time ($t_{1/2}$), and *pseudo*-second-order kinetic (k_2), for the photocatalytic degradation of PFH_xA over $Bi_{2-x}Zn_xWO_{6+\delta}$ photocatalysts.

The natural components of the water matrix, including inorganic ions, are recognized as potential competitors of active sites on the surface of a photocatalyst. Thus, additional photodegradation tests were conducted using sample Zn2.5 in the presence of Cl^-, NO_3^-, or PO_4^{3-}. As shown in Fig. 6b, the photocatalytic removal efficiency of PFH_xA was lowered in the presence of these inorganic anions. Particularly, the PO_4^{3-} ions were more active in competition with PFH_xA molecules on the surface of $Bi_{2-x}Zn_xWO_{6+\delta}$ photocatalysts, significantly reducing the photocatalytic removal efficiency of PFH_xA. Depending on the type of water matrix, the photocatalytic removal efficiency of PFH_xA can be varied due to the simultaneous existence of inorganic ions and organic molecules (dissolved organic matter). Fig. 6c presents the effect of the water matrix (distilled water – DW, tap water – TW, and treated wastewater – TWW) on the photocatalytic removal of PFH_xA over sample Zn2.5. It can be seen that the photocatalytic removal efficiency of PFH_xA was much higher in tap water in comparison to distilled water and treated wastewater possibly due to the simultaneous presence of Fe (49 mg L^{-1}) or Mg (22.9 mg L^{-1}) ions. Interestingly, the presence of Cl^- (35 mg L^{-1}) in treated wastewater did not reduce the photocatalytic removal efficiency of sample Zn2.5.

3.3. Photodegradation mechanism

To gain insights into the possible mechanism for the degradation of PFH_xA over $Bi_{2-x}Zn_xWO_{6+\delta}$ photocatalysts, trapping experiments were conducted using sample Zn2.5 in the presence of isopropyl alcohol – IPA (1000 mg L^{-1}), *p*-benzoquinone – PBQ (1 mg L^{-1}), and ethylenediaminetetraacetic acid disodium salt dihydrate – Na_2EDTA (100 mg L^{-1}) as scavengers of $^{\bullet}OH$, $O_2^{\bullet-}$, and h^+, respectively. Fig. 6d shows that the photodegradation of PFH_xA over $Bi_{2-x}Zn_xWO_{6+\delta}$ photocatalysts was mainly driven by the involvement of photo-excited holes and superoxide radicals. This is because the conduction band minimum and valence band maximum of Bi_2WO_6 shifted upward, preferentially generating $O_2^{\bullet-}$ radicals since the reduction potential of $O_2/O_2^{\bullet-}$ is −0.33 eV. Similarly, photo-excited holes and $O_2^{\bullet-}$ were found to be the major contributors to the photodegradation of fluoroquinolones over Mg-substituted Bi_2WO_6.[64] Interestingly, hydroxyl radicals were not involved in the photodegradation of PFH_xA according to the results of trapping experiments. It is then inferred that the direct electron transfer (DET) from PFH_xA is an important step. In fact, this evidence is in good agreement with the proposed mechanistic study.[65] It has been reported that the formation of the radical $C_nF^{\bullet}_{2n+1}$ is a determining step in the reaction.[65,66] Then, to complete the oxidation process, different chemical and redox steps took place, such as the reaction with holes, electrons, and $O_2^{\bullet-}$ as possible steps to react with $C_nF^{\bullet}_{2n+1}$ formed and continue the photocatalytic reaction (Fig. 8).

To understand the reaction pathway of the photodegradation of PFH_xA over $Bi_{2-x}Zn_xWO_{6+\delta}$ photocatalysts, LC-QTOF/MS operating in a scan mode was used. By applying collision energy equal to 0 eV, we attempt to minimize a possible fragmentation of PFH_xA in an MS source and to identify specific products of its photodegradation. As shown in Fig. 7a, the deprotonated molecular ion of m/z = 312.97 and an ion of m/z = 268.98, which are associated with the loss of CO_2 from the carboxyl group, and an ion of m/z = 68.99 delivered from fragment CF_3 were observed in each MS spectra. This suggests the partial decomposition of PFH_xA in an MS source instead of its degradation by photocatalysis. Generally, dealkylation is the main process that takes place during the photocatalytic removal of PFAS,[44] and longer PFAS are degraded into shorter ones.[67] Interestingly, fragments indicating the photodegradation of PFH_xA into short-chain PFAS, such as perfluoropentanoic acid (M_w = 264.05 g mol^{-1}) or perfluorobutanoic acid (M_w = 214.4 g mol^{-1}) were not found. However, a thorough inspection of MS spectra acquired for the photocatalytically treated samples confirms the presence of smaller fragments of m/z = 248.96, m/z = 226.98, and m/z = 180.97, which are associated with the loss of HF, CO, CO_2, and C_nF_m (Fig. 7b) and the formation of $[M–HF–CO_2]$-, $[M + H–CF_4]$- and $[M–CO + H_2–CF_5]$-fragments.[68] Decarboxylation and defluorination are the main possible routes for the transformation of PFAS during the photocatalytic processes.[69] The possible mechanism for the photodegradation of PFH_xA over Zn^{2+}substituted Bi_2WO_6 is shown in Fig. 8. The reusability of the synthesized photocatalyst (sample Zn2.5) for the degradation of PFH_xA in an aqueous solution was

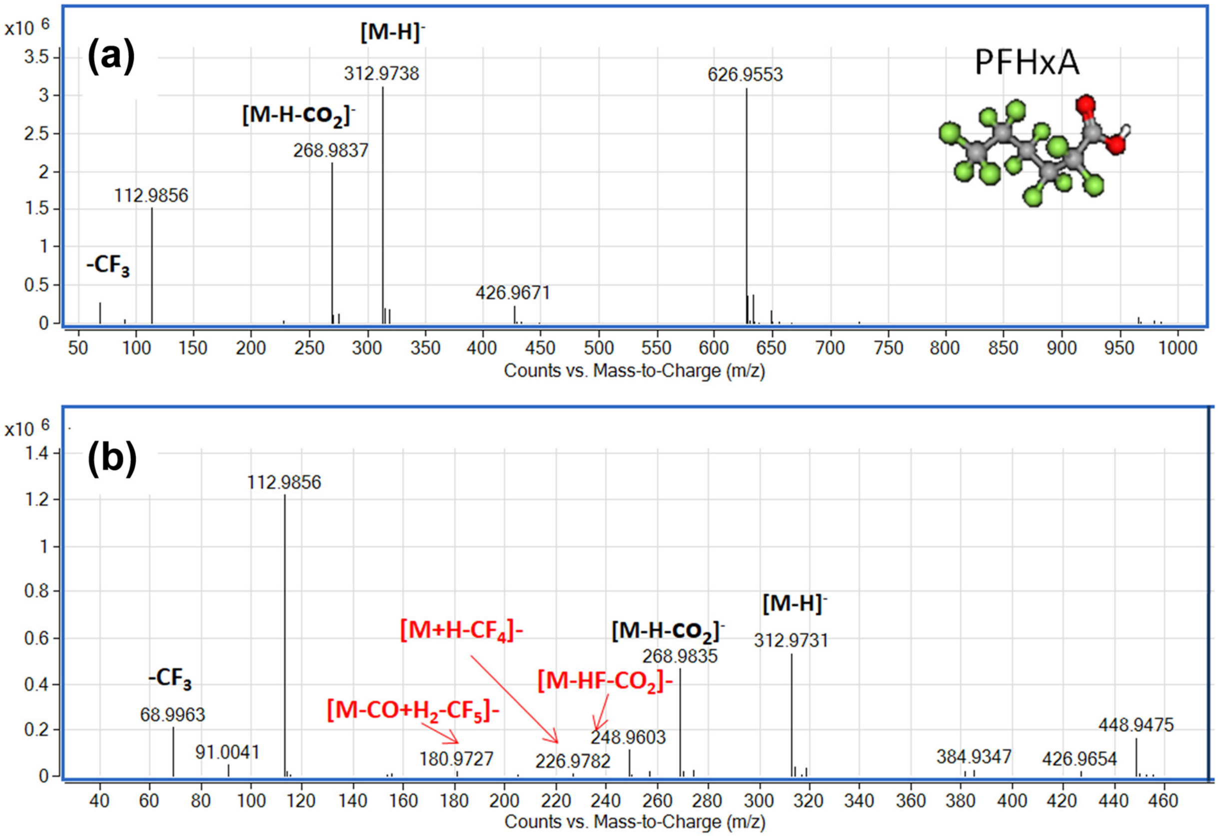

Fig. 7 Mass spectra of PFH_xA-containing water samples before (a) and after (b) photocatalytic treatment in the presence of sample Zn2.5.

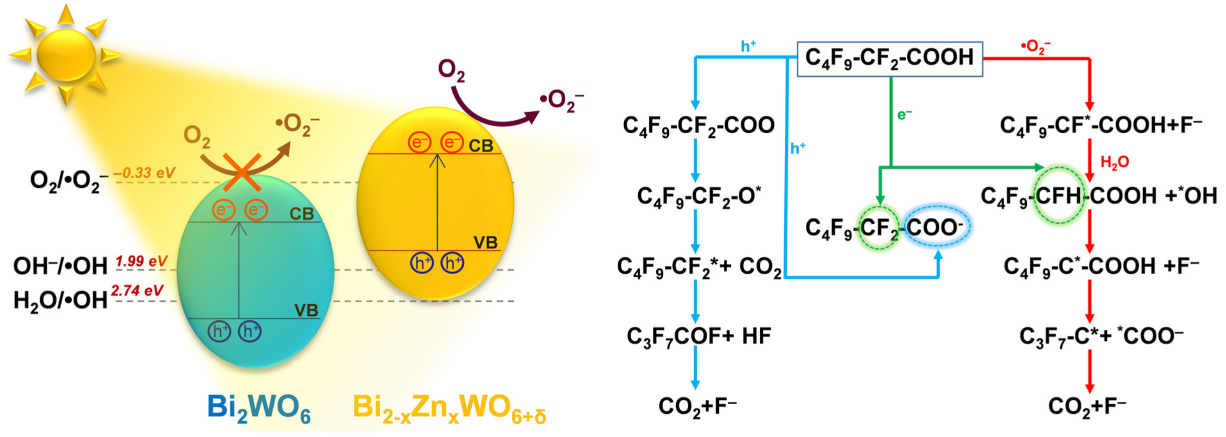

Fig. 8 Possible mechanism for the photodegradation of PFH_xA in an aqueous solution over the Zn^{2+}-substituted Bi_2WO_6 photocatalyst.

tested in four cycles. The obtained results in Fig. 6e revealed that sample Zn2.5 has good reusability since only a 27% reduction in photocatalytic activity after four runs was observed due to the loss of photocatalyst powders during collection and drying after each cycle.

3.4. Toxicity

The toxicity of photocatalytically treated water samples containing PFH_xA to *Aliivibrio fischeri* was estimated to be low (EC_{50} = 1.27 g).[70] The presence of PFH_xA in distilled water before and after photocatalytic treatment (Fig. 6f) did not affect the bioluminescence of *Aliivibrio fischeri*. However, slight toxicity (<20%) was observed in the water samples containing PFH_xA after photocatalytic treatment using sample Zn0. With the Zn^{2+} substituent, the toxicity was reduced, which needs further investigation to understand this phenomenon. The toxicity of the photocatalytically treated PFH_xA-containing TWW sample was significant (nearly 34%), inhibiting the bioluminescence of *Aliivibrio fischeri*.

4. Conclusions

Zn^{2+}-substituted Bi_2WO_6 has the potential to transform solar energy into redox reactions effectively because the partial substitution of Zn^{2+} for Bi^{3+} in the Bi_2WO_6 crystal lattice contracts the unit-cell volume, improves the absorption of visible light, and decreases the recombination of photo-excited charge carriers, favoring the photo-redox processes. The Bi_2WO_6 substituted with 2.5 at% Zn^{2+} differed from the unmodified Bi_2WO_6 by the possibility of generating $O_2^{\bullet-}$ due to the displacement of the conduction band to more negative potentials. The Zn^{2+}-substituted Bi_2WO_6 photocatalysts exhibited the highest pseudo-first-order kinetic constant for PFH_xA photodegradation (k_1 = 0.012 min^{-1}). Trapping experiments confirmed that photo-excited holes and superoxide radicals were the main reactive species involved in the photodegradation of PFH_xA. The direct electron transfer of PFH_xA was the important step and the reaction of holes, electrons, and $O_2^{\bullet-}$ with the $C_nF_{2n+1}^{\bullet}$ formed supported the photocatalytic oxidation reaction. Considering the complexity of wastewater, which simultaneously contains organic (dissolved organic matter) and inorganic substances (anions, such as nitrates, carbonates), the low photocatalytic efficiency in TTW still indicates the potential of the synthesized photocatalysts for practical application in the removal of PFAS under visible light irradiation. Furthermore, there is also a possibility to regenerate the used photocatalysts by heat treatment at temperatures above 157 °C, which is the boiling point of PFH_xA. Although the number of studies on the photocatalytic removal of PFAS has recently increased, the efficiency, stability, and scalability of such systems need to be further explored along with understanding their detailed mechanisms.

Author contributions

Mirabbos Hojamberdiev: conceptualization, investigation, methodology, validation, visualization, writing – original draft, writing – review & editing; Ana Laura Larralde: investigation, software, validation, writing – original draft; Ronald Vargas: formal analysis, investigation, software, validation, writing – original draft, writing – review & editing; Lorean Madriz: formal analysis, investigation, software, validation, writing – original draft, writing – review & editing; Kunio Yubuta: formal analysis, investigation, software, validation, writing – original draft; Lokesh Koodlur Sannegowda: investigation, writing – review & editing; Ilona Sadok: formal analysis, investigation, software, validation, writing – original draft; Agnieszka Krzyszczak-Turczyn: formal analysis, investigation, software, validation, writing – original draft; Patryk Oleszczuk: formal analysis, investigation, software, validation, writing – original draft; Bożena Czech: conceptualization, investigation, methodology, supervision, validation, visualization, writing – original draft, writing – review & editing.

Conflicts of interest

There are no conflicts to declare.

Acknowledgements

The authors would like to thank MPWIK Lublin and The John Paul II Catholic University of Lublin, Poland, for providing wastewater samples and giving access to services and research facilities, which were co-funded by the European Regional Development Fund (POPW.01.03.00-06-003/09-00), respectively. India-Uzbekistan Collaborative Grants (No. INT/Uzbek/P-21 and UZB-Ind-2021-91) are also acknowledged. The authors would like to thank Dipl. Phys. Christoph Fahrenson from ZELMI, TU Berlin, for his kind technical support in SEM analysis.

References

1 R. Mahinroosta and L. Senevirathna, A review of the emerging treatment technologies for PFAS contaminated soils, *J. Environ. Manage.*, 2020, **255**, 109896.

2 B. C. Crone, T. F. Speth, D. G. Wahman, S. J. Smith, G. Abulikemu, E. J. Kleiner and J. G. Pressman, Occurrence of Pre- and Polyfluoroalkyl Substances (PFAS) in Source Water and Their Treatment in Drinking Water, *Crit. Rev. Environ. Sci. Technol.*, 2019, **49**, 2359–2396.

3 J. L. Domingo and M. Nadal, Human exposure to per- and polyfluoroalkyl substances (PFAS) through drinking water: A review of the recent scientific literature, *Environ. Res.*, 2019, **177**, 108648.

4 F. Suja, B. K. Pramanik and S. M. Zain, Contamination, Bioaccumulation and Toxic Effects of Perfluorinated Chemicals (PFCs) in the Water Environment: A Review Paper, *Water Sci. Technol.*, 2009, **60**, 1533–1544.

5 United States Environmental Protection Agency, Technical Fact Sheet – Perfluorooctane Sulfonate (PFOS) and Perfluorooctanoic Acid (PFOA), EPA 505-F-17-001, United States Environmental Protection Agency, 2017 **https://19january2021snapshot.epa.gov/sites/static/files/2017-12/documents/ffrrofactsheet_contaminants_pfos_pfoa_11-20-17_508_0.pdf**, Per- and Polyfluoroalkyl Substances (PFAS) Proposed PFAS National Primary Drinking Water Regulation (Docket ID: EPA-HQ-OW-2022-0114), **https://www.epa.gov/sdwa/and-polyfluoroalkyl-substances-pfas**.

6 M. Wang, Y. Cai, B. Zhou, R. Yuan, Z. Chen and H. Chen, Removal of PFASs from water by carbon-based composite photocatalysis with adsorption and catalytic properties: A review, *Sci. Total Environ.*, 2022, **836**, 155652.

7 S. Kancharla, P. Alexandridis and M. Tsianou, Sequestration of per- and polyfluoroalkyl substances (PFAS) by adsorption: Surfactant and surface aspects, *Curr. Opin. Colloid Interface Sci.*, 2022, **58**, 101571.

8 D. M. Wanninayake, Comparison of currently available PFAS remediation technologies in water: A review, *J. Environ. Manage.*, 2021, **283**, 111977.

9 A. L. Luz, J. K. Anderson, P. Goodrum and J. Durda, Perfluorohexanoic acid toxicity, part I: Development of a chronic human health toxicity value for use in risk assessment, *Regul. Toxicol. Pharmacol.*, 2019, **103**, 41–55.

10 J. K. Anderson, A. L. Luz, P. Goodrum and J. Durda, Perfluorohexanoic acid toxicity, part II: Application of human health toxicity value for risk characterization, *Regul. Toxicol. Pharmacol.*, 2019, **103**, 10–20.

11 *Annex XV Report: Proposal for Identification of a Substance of Very High Concern on the Basis of the Criteria Set Out in REACH Article 57*, Identification of Undecafluorohexanoic Acid and its Ammonium Salt as SVHC.

12 E. T. Hernandez, B. Koo, L. E. Sofen, R. Amin, R. K. Togashi, A. I. Lall, D. J. Gisch, B. J. Kern, M. A. Rickard and M. B. Francis, Proteins as adsorbents for PFAS removal from water, *Environ. Sci.: Water Res. Technol.*, 2022, **8**, 1188–1194.

13 T. Jin, M. Peydayesh, H. Joerss, J. Zhou, S. Bolisetty and R. Mezzenga, Amyloid fibril-based membranes for PFAS removal from water, *Environ. Sci.: Water Res. Technol.*, 2021, **7**, 1873–1884.

14 T. H. Boyer, Y. Fang, A. Ellis, R. Dietz, Y. J. Choi, C. E. Schaefer, C. P. Higgins and T. J. Strathmann, Anion exchange resin removal of per- and polyfluoroalkyl substances (PFAS) from impacted water: A critical review, *Water Res.*, 2021, **200**, 117244.

15 T. Buckley, K. Karanam, X. Xu, P. Shukla, M. Firouzi and V. Rudolph, Effect of mono- and di-valent cations on PFAS removal from water using foam fractionation – A modelling and experimental study, *Sep. Purif. Technol.*, 2022, **286**, 120508.

16 M. B. Ahmed, Md. M. Alam, J. L. Zhou, B. Xu, Md. A. H. Johir, A. K. Karmakar, Md. S. Rahman, J. Hossen, A. T. M. K. Hasan and M. A. Moni, Advanced treatment technologies efficacies and mechanism of per- and poly-fluoroalkyl substances removal from water, *Process Saf. Environ. Prot.*, 2020, **136**, 1–14.

17 D. Zhang, Q. Luo, B. Gao, S.-Y. D. Chiang, D. Woodward and Q. Huang, Sorption of perfluorooctanoic acid, perfluorooctane sulfonate and perfluoroheptanoic acid on granular activated carbon, *Chemosphere*, 2016, **144**, 2336–2342.

18 Q. Zhuo, S. Deng, B. Yang, J. Huang and G. Yu, Efficient Electrochemical Oxidation of Perfluorooctanoate Using a Ti/SnO_2-Sb-Bi Anode, *Environ. Sci. Technol.*, 2011, **45**, 2973–2979.

19 X. Li, P. Zhang, L. Jin, T. Shao, Z. Li and J. Cao, Efficient Photocatalytic Decomposition of Perfluorooctanoic Acid by Indium Oxide and Its Mechanism, *Environ. Sci. Technol.*, 2012, **46**, 5528–5534.

20 R. R. Giri, H. Ozaki, T. Okada, S. Taniguchi and R. Takanami, Factors influencing UV photodecomposition of perfluorooctanoic acid in water, *Chem. Eng. J.*, 2012, **180**, 197–203.

21 H. V. Lutze, J. Brekenfeld, S. Naumov, C. von Sonntag and T. C. Schmidt, Degradation of perfluorinated compounds by sulfate radicals – New mechanistic aspects and economical considerations, *Water Res.*, 2018, **129**, 509–519.

22 C. D. Vecitis, Y. Wang, J. Cheng, H. Park, B. T. Mader and M. R. Hoffmann, Sonochemical Degradation of Perfluorooctanesulfonate in Aqueous Film-Forming Foams, *Environ. Sci. Technol.*, 2010, **44**, 432–438.

23 Z. Zhang, J.-J. Chen, X.-J. Lyu, H. Yin and G.-P. Sheng, Complete mineralization of perfluorooctanoic acid (PFOA) by γ-irradiation in aqueous solution, *Sci. Rep.*, 2014, **4**, 7418.

24 P. J. Krusic, A. A. Marchione and D. C. Roe, Gas-phase NMR studies of the thermolysis of perfluorooctanoic acid, *J. Fluorine Chem.*, 2005, **126**, 1510–1516.

25 H. Hori, M. Murayama and S. Kutsuna, Oxygen-induced efficient mineralization of perfluoroalkylether sulfonates in subcritical water, *Chemosphere*, 2009, **77**, 1400–1405.

26 H. Obo, N. Takeuchi and K. Yasuoka, Decomposition of perfluorooctanesulfonate (PFOS) by multiple alternating argon plasmas in bubbles with gas circulation, *Int. J. Plasma Environ. Sci. Technol.*, 2015, **9**, 62–68.

27 S. Wang, Q. Yang, F. Chen, J. Sun, K. Luo, F. Yao, X. Wang, D. Wang, X. Li and G. Zeng, Photocatalytic degradation of perfluorooctanoic acid and perfluorooctane sulfonate in water: A critical review, *Chem. Eng. J.*, 2017, **328**, 927–942.

28 H. Tang, Q. Xiang, M. Lei, J. Yan, L. Zhu and J. Zou, Efficient degradation of perfluorooctanoic acid by UV–Fenton process, *Chem. Eng. J.*, 2012, **184**, 156–162.

29 Y. Wang and P. Zhang, Photocatalytic decomposition of perfluorooctanoic acid (PFOA) by TiO_2 in the presence of oxalic acid, *J. Hazard. Mater.*, 2011, **192**, 1869–1875.

30 Z. Li, P. Zhang, T. Shao and X. Li, In_2O_3 nanoporous nanosphere: A highly efficient photocatalyst for decomposition of perfluorooctanoic acid, *Appl. Catal., B*, 2012, **125**, 350–357.

31 Z. Song, X. Dong, N. Wang, L. Zhu, Z. Luo, J. Fang and C. Xiong, Efficient photocatalytic defluorination of perfluorooctanoic acid over BiOCl nanosheets via a hole direct oxidation mechanism, *Chem. Eng. J.*, 2017, **317**, 925–934.

32 T. Shao, P. Zhang, L. Jin and Z. Li, Photocatalytic decomposition of perfluorooctanoic acid in pure water and sewage water by nanostructured gallium oxide, *Appl. Catal., B*, 2013, **142–143**, 654–661.

33 W. Ding, X. Tan, G. Chen, J. Xu, K. Yu and Y. Huang, Molecular-Level Insights on the Facet-Dependent Degradation of Perfluorooctanoic Acid, *ACS Appl. Mater. Interfaces*, 2021, **13**, 41584–41592.

34 N. Zhang, R. Ciriminna, M. Pagliaro and Y.-J. Xu, Nanochemistry-derived Bi_2WO_6 nanostructures: towards production of sustainable chemicals and fuels induced by visible light, *Chem. Soc. Rev.*, 2014, **43**, 5276–5287.

35 L. Zhang, H. Wang, Z. Chen, P. K. Wong and J. Liu, Bi_2WO_6 micro/nano-structures: Synthesis, modifications and visible-light-driven photocatalytic applications, *Appl. Catal., B*, 2011, **106**, 1–13.

36 O. Núñez, L. Madriz, D. Carvajal, J. Tatá and R. Vargas, Unprecedented large solvent (H_2O vs D_2O) isotope effect in semiconductors photooxidation, *J. Phys. Org. Chem.*, 2019, **32**, e3952.

37 M. Arif, M. Zhang, J. Yao, H. Yin, P. Li, I. Hussain and X. Liu, Layer-assembled 3D Bi_2WO_6 hierarchical architectures by Ti-doping for enhanced visible-light driven photocatalytic and photoelectrochemical performance, *J. Alloys Compd.*, 2019, **792**, 878–893.

38 V. Koteski, J. Belošević-Čavor, V. Ivanovski, A. Umićević and D. Toprek, Ab initio calculations of the optical and electronic properties of Bi_2WO_6 doped with Mo, Cr, Fe, and Zn on the W–lattice site, *Appl. Surf. Sci.*, 2020, **515**, 146036.

39 F. Ren, J. Zhang and Y. Wang, Enhanced photocatalytic activities of Bi_2WO_6 by introducing Zn to replace Bi lattice sites: a first-principles study, *RSC Adv.*, 2015, **5**, 29058–29065.

40 M. Hojamberdiev, Z. C. Kadirova, E. Zahedi, D. Onna, M. C. Marchi, G. Zhu, N. Matsushita, M. Hasegawa, S. A. Bilmes and K. Okada, Tuning the morphological structure, light absorption, and photocatalytic activity of Bi_2WO_6 and Bi_2WO_6-BiOCl through cerium doping, *Arabian J. Chem.*, 2020, **13**, 2844–2857.

41 J. Rodríguez-Carvajal, *FULLPROF: A Program for Rietveld Refinement and Pattern Matching Analysis, Abstract of the Satellite Meeting on Powder Diffraction of the XV Congress of the IUCr*, Toulouse, France, 1990, p. 127.

42 M. Hojamberdiev, B. Czech, A. Wasilewska, A. Boguszewska-Czubara, K. Yubuta, H. Wagata, S. S. Daminova, Z. C. Kadirova and R. Vargas, Detoxifying SARS-CoV-2 antiviral drugs from model and real wastewaters by industrial waste-derived multiphase photocatalysts, *J. Hazard. Mater.*, 2022, **429**, 128300.

43 L. S. Gómez-Velázquez, L. Madriz, M. Rigoletto, E. Laurenti, M. Bizarro, M. L. Dell'Arciprete and M. C. González, Structural and Physicochemical Properties of Carbon Nitride Nanoparticles via Precursor Thermal Treatment: Effect on Methyl Orange Photocatalytic Discoloration, *ACS Appl. Nano Mater.*, 2023, **6**, 14049–14062.

44 S. Taniyasu, N. Yamashita, E. Yamazaki, G. Petrick and K. Kannan, The environmental photolysis of perfluorooctanesulfonate, perfluorooctanoate, and related fluorochemicals, *Chemosphere*, 2013, **90**, 1686–1692.

45 *Microtox® Acute Toxicity Manual*, Modern Water Inc., **https://www.modernwater.com/wp-content/uploads/2022/09/MW-Microtox-Acute-Toxicity-Manual-Brochure-WEB.pdf**.

46 R. D. Shannon, Revised effective ionic radii and systematic studies of interatomic distances in halides and chalcogenides, *Acta Crystallogr., Sect. A: Cryst. Phys., Diffr., Theor. Gen. Crystallogr.*, 1976, **32**, 751–767.

47 M. Hojamberdiev, K.-I. Katsumata, N. Matsushita and K. Okada, Preparation of Bi_2WO_6- and BiOI-allophane composites for efficient photodegradation of gaseous acetaldehyde under visible light, *Appl. Clay Sci.*, 2014, **101**, 38–43.

48 M. Hojamberdiev, Z. C. Kadirova, R. V. Gonçalves, K. Yubuta, N. Matsushita, K. Teshima, M. Hasegawa and K. Okada, Reduced graphene oxide-modified Bi_2WO_6/BiOI composite for the effective photocatalytic removal of organic pollutants and molecular modeling of adsorption, *J. Mol. Liq.*, 2018, **268**, 715–727.

49 M. Hojamberdiev, Z. C. Kadirova, Y. Makinose, G. Zhu, S. Emin, N. Matsushita, M. Hasegawa, M. Hasegawa and K. Okada, Involving $CeVO_4$ in improving the photocatalytic activity of a Bi_2WO_6/allophane composite for the degradation of gaseous acetaldehyde under visible light, *Colloids Surf., A*, 2017, **529**, 600–612.

50 D. Saha, E. D. Bøjesen, A. H. Mamakhel and B. B. Iversen, Why Does Bi_2WO_6 Visible-Light Photocatalyst Always Form as Nanoplatelets?, *Inorg. Chem.*, 2020, **59**, 9364–9373.

51 L. Zhang, W. Wang, Z. Chen, L. Zhou, H. Xu and W. Zhu, Fabrication of flower-like Bi_2WO_6 superstructures as high performance visible-light driven photocatalysts, *J. Mater. Chem.*, 2007, **17**, 2526–2532.

52 H. Fu, C. Pan, W. Yao and Y. Zhu, Visible-Light-Induced Degradation of Rhodamine B by Nanosized Bi_2WO_6, *J. Phys. Chem. B*, 2005, **109**, 22432–22439.

53 M. Hojamberdiev, K.-I. Katsumata, K. Morita, S. A. Bilmes, N. Matsushita and K. Okada, One-step hydrothermal synthesis and photocatalytic performance of $ZnWO_4$/Bi_2WO_6 composite photocatalysts for efficient degradation of acetaldehyde under UV light irradiation, *Appl. Catal., A*, 2013, **457**, 12–20.

54 M. Hojamberdiev, R. M. Prasad, K. Morita, M. A. Schiavon and R. Riedel, Polymer-derived mesoporous SiOC/ZnO nanocomposite for the purification of water contaminated with organic dyes, *Microporous Mesoporous Mater.*, 2012, **151**, 330–338.

55 L. X. Lovisa, T. B. O. Nunes, R. R. Y. O. V. Wilson, E. Longo, M. D. Teodoro, M. R. D. Bomio and F. V. Motta, Synthesis and evaluation of photocatalytic and photoluminescent properties of Zn^{2+}-doped Bi_2WO_6, *Dalton Trans.*, 2022, **51**, 17700–17710.

56 A. Etogo, R. Liu, J. Ren, L. Qi, C. Zheng, J. Ning, Y. Zhong and Y. Hu, Facile one-pot solvothermal preparation of Mo-doped Bi_2WO_6 biscuit-like microstructures for visible-light-driven photocatalytic water oxidation, *J. Mater. Chem. A*, 2016, **4**, 13242–13250.

57 L. Madriz, J. Tatá, D. Carvajal, O. Núñez, B. R. Scharifker, J. Mostany, C. Borrás, F. M. Cabrerizo and R. Vargas, Photocatalysis and photoelectrochemical glucose oxidation on Bi_2WO_6: conditions for the concomitant H_2 production, *Renewable Energy*, 2020, **152**, 974–983.

58 C. Bhattacharya, H. C. Lee and A. J. Bard, Rapid Screening by Scanning Electrochemical Microscopy (SECM) of Dopants for Bi_2WO_6 Improved Photocatalytic Water Oxidation with Zn Doping, *J. Phys. Chem. C*, 2013, **117**, 9633–9640.

59 O. Núñez and R. Vargas, The interplay between RedOx, photophysics and surface process in Bi2WO6 photocatalyst, in *A Closer Look at Chemical Kinetics*, ed. V. Martinez-Luaces, Nova Science Publishers, 2023, pp. 205–222.

60 F. Rao, G. Zhu, M. Hojamberdiev, W. Zhang, S. Li, J. Gao, F. Zhang, Y. Huang and Y. Huang, Uniform Zn^{2+}-Doped BiOI Microspheres Assembled by Ultrathin Nanosheets with Tunable Oxygen Vacancies for Super-Stable Removal of NO, *J. Phys. Chem. C*, 2019, **123**, 16268–16280.

61 H. Lv, Y. Liu, J. Guang, Z. Ding and J. Wan, Shape-selective synthesis of Bi_2WO_6 hierarchical structures and their morphology-dependent photocatalytic activities, *RSC Adv.*, 2016, **6**, 80226–80233.

62 Z. Li, P. Zhang, J. Li, T. Shao and L. Jin, Synthesis of In_2O_3-graphene composites and their photocatalytic performance towards perfluorooctanoic acid decomposition, *J. Photochem. Photobiol., A*, 2013, **271**, 111–116.

63 M. Li, Z. Yu, Q. Liu, L. Sun and W. Huang, Photocatalytic decomposition of perfluorooctanoic acid by noble metallic nanoparticles modified TiO_2, *Chem. Eng. J.*, 2016, **286**, 232–238.

64 F. Zhu, Y. Lv, J. Li, J. Ding, X. Xia, L. Wei, J. Jiang, G. Zhang and Q. Zhao, Enhanced visible light photocatalytic performance with metal-doped Bi_2WO_6 for typical fluoroquinolones degradation: Efficiencies, pathways and mechanisms, *Chemosphere*, 2020, **252**, 126577.

65 J. Radjenovic, N. Duinslaeger, S. S. Avval and B. P. Chaplin, Facing the Challenge of Poly- and Perfluoroalkyl Substances in Water: Is Electrochemical Oxidation the Answer?, *Environ. Sci. Technol.*, 2020, **54**, 14815–14829.

66 Y. S. Khalid, S. N. Misal, S. Mehraeen and B. P. Chaplin, Reactive-Transport Modeling of Electrochemical Oxidation of Perfluoroalkyl Substances in Porous Flow-through Electrodes, *ACS ES&T Engg*, 2022, **2**, 713–725.

67 B. Xu, J. L. Zhou, A. Altaee, M. B. Ahmed, M. A. H. Johir, J. Ren and X. Li, Improved photocatalysis of perfluorooctanoic acid in water and wastewater by Ga_2O_3/UV system assisted by peroxymonosulfate, *Chemosphere*, 2020, **239**, 124722.

68 M. Altarawneh, M. H. Almatarneh and B. Z. Dlugogorski, Thermal decomposition of perfluorinated carboxylic acids: Kinetic model and theoretical requirements for PFAS incineration, *Chemosphere*, 2022, **286**, 131685.

69 C. Fu, X. Xu, C. Zheng, X. Liu, D. Zhao and W. Qiu, Photocatalysis of aqueous PFOA by common catalysts of In_2O_3, Ga_2O_3, TiO_2, CeO_2 and CdS: influence factors and mechanistic insights, *Environ. Geochem. Health*, 2022, **44**, 2943–2953.

70 E. Mulkiewicz, B. Jastorff, A. C. Składanowski, K. Kleszczyński and P. Stepnowski, Evaluation of the acute toxicity of perfluorinated carboxylic acids using eukaryotic cell lines, bacteria and enzymatic assays, *Environ. Toxicol. Pharmacol.*, 2007, **23**, 279–285.